Available online at www.sciencedirect.com
ScienceDirect
Acta Materialia 59 (2011) 1619–1631
Acta MATERIALIA
www.elsevier.com/locate/actamat

Enhanced solid solution effects on the strength of nanocrystalline alloys

Timothy J. Rupert, Jonathan C. Trenkle, Christopher A. Schuh *

Department of Materials Science and Engineering, Massachusetts Institute of Technology, 77 Massachusetts Avenue, Cambridge, MA 02139, USA

Received 27 October 2010; received in revised form 8 November 2010; accepted 9 November 2010
Available online 8 December 2010

Abstract

Solid solution strengthening in nanocrystalline alloys is studied using sputtered Ni–W as a model system. In the composition range of 0–20 at.% W, the sputtered alloys have a nanocrystalline structure with a grain size that is independent of composition. Nanoindentation of these alloys shows that solute addition increases strength to very high levels, almost in proportion to the solute content. This behavior is not expected based on traditional solid solution strengthening mechanistic models of local dislocation pinning at solute atoms, but can be explained by further considering a global effect of solute on the average properties of the Ni lattice. The new strengthening term arises by considering grain boundaries as pinning points for dislocation motion in nanocrystalline materials and incorporating the effect of solutes on such a mechanism. Our discussion surrounding Ni–W also provides insights into other solid solution nanocrystalline systems, a variety of which we show can be accurately described using the same concept. These developments also explain the origin of solid solution softening in some nanocrystalline alloys.

Keywords: Solute strengthening; Nanocrystalline metals; Mechanical behavior; Nanoindentation; Thin films

1. Introduction

Nanocrystalline metals have been the focus of intense research efforts in recent years due to their novel deformation physics. As grain size reaches the nanometer range, traditional intragranular dislocation mechanisms for plasticity are suppressed and deformation becomes dominated by grain boundary processes such as grain boundary dislocation emission [1–3], grain boundary sliding [4,5], and grain boundary migration [6–8]. The emergence of these novel mechanisms is not only scientifically interesting, but also has a profound effect on engineering properties; for example, improved strength [9,10], fatigue resistance [11], and wear resistance [12–14] have all been reported for grain sizes below about 100 nm where the mechanisms begin to shift, as has an increased rate dependence [15,16] and pressure dependence [17,18] of strength.

In practice, nanocrystalline systems with significant alloying additions are more useful than their pure metal counterparts, due to the increased thermal stability and grain size control that can be realized with alloying additions. A number of pure nanocrystalline metals experience room temperature grain growth [19,20], with a corresponding degradation of their properties. Others have been reported to coarsen under load or in service conditions [21,22], limiting the possibility of prolonged use in application. On the other hand, recent work has shown that the addition of alloying elements can produce stabilized nanocrystalline metals, either through classical kinetic constraints on coarsening or through thermodynamic reduction of the driving forces for coarsening [23,24]. For example, electrodeposited Ni–W alloys have nanocrystalline grain structures that do not coarsen appreciably when heated to temperatures up to ~500 °C [25]. In these Ni–W alloys, W additions exhibit a subtle tendency to segregate to grain boundaries, where they lower the grain boundary energy and bring the system closer to thermodynamic equilibrium [26]. As a result of this segregation tendency, alloy-

* Corresponding author.
E-mail address: schuh@mit.edu (C.A. Schuh).

1359-6454/$36.00 © 2010 Acta Materialia Inc. Published by Elsevier Ltd. All rights reserved.
doi:10.1016/j.actamat.2010.11.026

ing additions also allow grain size to be precisely controlled during a process of electrodeposition, with W promoting grain refinement [27].

In light of these considerations, we view alloying elements as a key ingredient for almost any commercializable nanocrystalline metal. Therefore, a more complete understanding of alloying effects on the novel deformation mechanisms that dominate at the finest grain sizes is needed. What complicates this task is that when an alloying addition and a nanoscale grain size are present, both have potentially significant effects on properties and the two are difficult to decouple systematically because composition affects structure. For example, in the electrodeposited Ni–W alloys mentioned above, grain size is intimately tied to composition [27], and changing one of these variables tends to cause changes in the other (at least in the as-deposited state). A number of other nanocrystalline alloys, such as Ni–P [28], Pd–Zr [29], and Ni–Fe [30], exhibit a similar dependence of grain size on composition. Detailed studies that isolate the effects of grain size and composition for various systems (solid solution, phase separating, etc.) are needed.

There have been a number of papers that have addressed alloying effects on the mechanical properties of nanocrystalline metals [31–33]. These are for the most part somewhat speculative, again because they are generally unable to separate the effects of composition and grain size. At the same time, it is only relatively recently that detailed understanding of the deformation mechanisms of nanocrystalline pure metals has emerged [3,34–37], and many early studies of alloying effects could not benefit from the insights of those works. We suggest that the understanding of deformation mechanisms in pure metals with nanoscale grain sizes is now sufficiently mature that it may be possible to begin to specifically isolate the effects of alloying additions upon those mechanisms. In the present paper, we provide some initial steps towards this goal, by developing a set of idealized solid solution nanocrystalline specimens of Ni–W. After exploring the processing space for these alloys by magnetron sputtering, we prepare a set of samples that all have the same grain size (~20 nm), but contain solid solution additions spanning a broad range of 0–20 at.% W. The mechanical properties of these alloys are investigated to provide insight into solid solution strengthening of nanocrystalline metals, at a grain size where deformation is dominated by grain boundary processes. The results are then generalized to other solid solutions, and broad conclusions about the role of solution alloying on the strength of nanocrystalline alloys are developed.

2. Materials and methods

As noted above, Ni–W is a well-studied nanocrystalline system, especially in electrodeposited form. However, the grain size and composition of Ni–W electrodeposits are linked monotonically; in fact, composition is used to control grain size [27]. Here, we seek an alternative route for producing nanocrystalline Ni–W alloys where grain size is not controlled purely by composition. Specifically, we employ sputter deposition, since this highly energetic deposition process leads to kinetic limitations on grain size. The existing literature on sputter deposited Ni–W suggests that face-centered-cubic (fcc), amorphous, or body-centered-cubic (bcc) phases can be produced [38–43], although detailed microstructural characterization spanning a wide range of compositions does not appear to exist. Alloys with a broad range of compositions were deposited using an ATC magnetron sputtering system (AJA International, Scituate, MA). Prior to deposition, the chamber was evacuated to $<10^{-6}$ torr and then backfilled with Ar to 4 m torr, which was maintained throughout deposition. Direct current magnetron sputtering was used; to vary the W content in the alloys, the relative currents to the W and Ni targets were adjusted. To identify a composition range where grain size is constant, alloys for transmission electron microscopy (TEM) were directly deposited onto Ni TEM grids with a carbon-stabilized resin backing (Ted Pella Inc., Redding, CA) to a thickness of ~50 nm so that no subsequent sample preparation was necessary; these will be referred to throughout as the "thin" samples. Thicker coatings (thickness ~1 μm) were deposited onto Si wafers for structural characterization by X-ray diffraction (XRD) and for mechanical testing by nanoindentation; these will be referred to as "thick" samples.

The thin specimens were examined using a JEOL 2010 TEM operated at 200 kV. The phases present in each sample were determined using bright field images and electron diffraction patterns. Grain size (d) was measured by manually tracing individual grains and determining the circular equivalent diameter. XRD of the thick specimens was performed on a PANalytical X'Pert Pro diffractometer with a Cu Kα radiation source operated at 45 kV and 40 mA. XRD profiles were used for phase determination, to measure lattice parameter, and to estimate the average grain size to within ±15% by applying the Scherrer equation [44] to the (1 1 1) peak after subtracting instrumental broadening. The composition of each alloy was measured by energy dispersive spectroscopy (EDS) in a Leo 438VP scanning electron microscope (SEM) operated at 20 kV.

Mechanical properties were measured by instrumented nanoindentation using a Hysitron Ubi1 with a diamond Berkovich tip. The Oliver–Pharr method [45] was used to extract hardness and reduced modulus from load–displacement curves, using a tip area function which was carefully calibrated on fused silica. All tests were carried out at constant indentation strain rates, $\dot{\varepsilon}$, given by [46]:

$$\dot{\varepsilon} = \frac{1}{h}\frac{\partial h}{\partial t} = \frac{1}{2}\left(\frac{1}{P}\frac{\partial P}{\partial t}\right) \quad (1)$$

where h is indentation depth, t is time, and P is applied load. After loading at the strain rate of interest, the sample was unloaded to 20% of the maximum load and a 10 s hold was used to characterize instrumental drift. A maximum load of 2 mN was used, corresponding to indentation

depths <100 nm for all films, less than 10% of the total film thickness in order to avoid substrate effects. Each data point presented is the average of data extracted from a minimum of 100 indentations.

3. Structural characterization

3.1. Characterization of the thin specimens

In total, 10 thin specimens with W content ranging from 0 to 66.3 at.% were produced for TEM investigation. Fig. 1 presents TEM micrographs from selected specimens across the range of deposited compositions, while Table 1 provides W content, phases present, and grain size for all of the specimens. The pure Ni sample (Fig. 1a) exhibits a nanocrystalline structure with a grain size of $d \sim 10$ nm and selected-area electron diffraction patterns confirm the phase to be fcc. As W content increases to ~20 at.%, this same microstructure (nanocrystalline fcc, $d \sim 10$ nm) is observed, with representative TEM images from the 8.9 and 19 at.% W alloys shown in Fig. 1b and c, respectively. No evidence of stored dislocation networks was found in the grain interiors for any of the specimens, consistent with other reports of dislocation-free nanocrystalline microstructures [2,47]. The electron diffraction patterns for the 8.9 and 19 at.% W alloys (insets to Fig. 1b and c) show that the lattice parameter increases as the larger W atoms are substituted into the fcc lattice and that there is no obvious in-plane texture, with uniform brightness around each diffraction ring. Some slight (2 2 0) out-of-plane texture may be present in the 19 at.% W sample, with the (2 2 0) ring being only slightly less intense than the (1 1 1) ring in Fig. 1c, but this texture appears to be subtle. Fig. 2 presents the grain size distribution of a sample with 13.3 at.% W, which reveals an average grain size of 10 nm.

Further increasing the W content to 24.2 at.% still results in a nanocrystalline fcc structure, but the grain size and grain morphologies now change. Fig. 1d presents a TEM image of this alloy, where an abnormally large grain (diameter of ~70 nm) with non-equilibrium morphology can be observed in the upper right corner and a number of medium-sized grains with diameters above 20 nm are seen throughout. For compositions with more than ~30 at.% W, an amorphous phase is observed. A dual-phase structure containing nanocrystals embedded in an amorphous matrix is found for 30.8 at.% W, as presented in Fig. 1e. If W content is increased to 39.4 at.%, the structure is found to be fully amorphous, as shown by the featureless TEM image in Fig. 1f. Such a completely amorphous structure was observed for all of the samples with ~40–66 at.% W. The emergence of an amorphous phase at the compositions shown here suggests an apparent solubility limit between approximately 24 and 30 at.% W. While the equilibrium phase diagram predicts a solubility limit of only ~12 at.% W [48], the higher apparent solubility observed here is expected for two reasons. First, nanocrystalline systems have higher solubility limits owing to relaxation of size mismatch strains at grain boundaries and related segregation effects [49,50], and second, deposition processing leads to non-equilibrium structures and can by itself promote some supersaturation [51,52]. Our results align with those from electrodeposited Ni–W, where up to ~27 at.% W was incorporated into a solid solution fcc phase [27].

Evidence of the transitions between nanocrystalline, dual-phase amorphous–nanocrystalline, and amorphous structures described above can also be seen in the electron diffraction patterns presented in the insets to Fig. 1. Fig. 1b–d shows diffraction patterns from alloys with 8.9, 19, and 24.2 at.% W, respectively. All of the diffraction

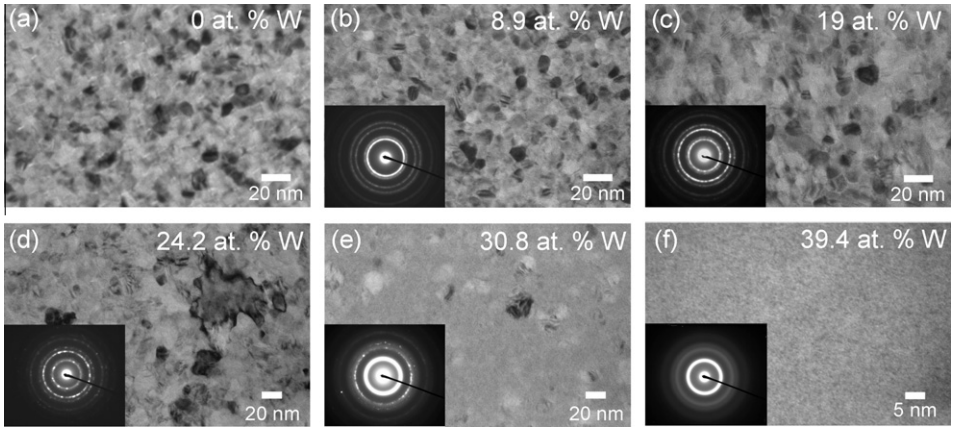

Fig. 1. TEM images of sputtered Ni–W films. (a–c) A nanocrystalline fcc structure with a constant grain size of ~10 nm is observed for 0–19 at.% W. (d) A nanocrystalline fcc structure with a larger grain size and some irregular grains is found at 24.2 at.% W. (e) An amorphous–nanocrystalline composite structure is found at 30.8 at.% W. (f) A fully amorphous structure is observed at 39.4 at.% W and above. The electron diffraction patterns (inset) also provide evidence of the transitions between nanocrystalline, dual-phase amorphous–nanocrystalline, and amorphous structures. In (b–d), all diffraction rings can be indexed to the fcc nanocrystalline phase. More discrete diffraction spots are seen in (d) due to the larger grain size. (e) The broad halo characteristic of an amorphous phase is present, as well as discrete spots from coherent diffraction of an fcc phase. (f) Broad diffraction rings are present in the pattern from the fully amorphous sample. Closer inspection of the diffraction pattern suggests that some medium range order may be present.

Table 1
Microstructure of sputtered thin Ni–W specimens produced for TEM investigation (thickness ~50 nm).

W content (at.%)	Phases present	Average TEM grain size (nm)
0	Nanocrystalline fcc	10 ± 3
4.8	Nanocrystalline fcc	9 ± 3
8.9	Nanocrystalline fcc	10 ± 2
13.3	Nanocrystalline fcc	10 ± 3
19	Nanocrystalline fcc	11 ± 4
24.2	Nanocrystalline fcc	24 ± 16
30.8	Amorphous + nanocrystalline fcc	19 ± 10
39.4	Amorphous	–
50.3	Amorphous	–
66.3	Amorphous	–

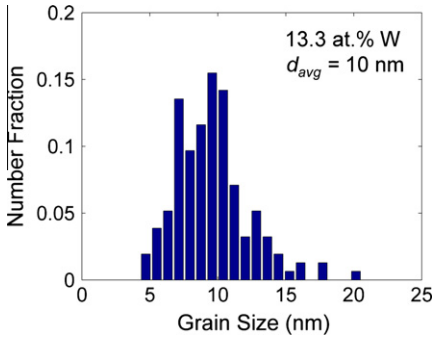

Fig. 2. Grain size distribution measured of the 13.3 at.% W alloy. The distribution has an average grain size of 10 nm.

rings in these patterns can be attributed to an fcc solid solution, although more discrete spots are seen in Fig. 1d due to the larger grain size of the 24.2 at.% W specimen. In Fig. 1e (30.8 at.% W), the broad halo characteristic of an amorphous phase is present, as well as discrete spots from coherent diffraction of an fcc phase. Finally, the pattern from the 39.4 at.% W specimen presented in Fig. 1f contains only broad diffraction halos. Closer inspection of this pattern reveals that what appears to be the second halo at first glance is in fact two diffuse rings which are slightly overlapping, as has been observed in some amorphous alloys with medium range order on a length scale of 1–2 nm [53].

3.2. Characterization of the thick solid solution specimens

Based on the results in Figs. 1 and 2, we may identify a composition range (up to about 20 at.% W) over which we produce a single-phase solid solution with a constant grain size of ~10 nm. Accordingly, we now focus the remainder of the study on a select group of specimens from within this range: four alloy compositions (0, 9.1, 13.6, and 20 at.% W) were sputter deposited to ~1 μm thickness for further testing. The grain sizes of these thicker films, determined by XRD and included in Table 2, are all about the same at $d = 18 \pm 2$ nm. Note that this grain size is slightly larger than we obtained in the thin samples examined in TEM ($d \sim 10$ nm), which reflects a slight increase in the average grain size with film thickness, as has been observed for other sputtered metals [47,54]. No evidence of any out-of-plane texture was observed in the XRD patterns for any of the specimens. The subtle (2 2 0) texture observed in the thin specimen with a W content of ~20 at.% disappears as film thickness is increased.

The lattice parameter of each thick specimen was also calculated from XRD determination of the (1 1 1) peak position. Our measured values agree well with the experimentally established linear relation between lattice parameter and composition for Ni–W alloys [55]:

$$a = a_{\mathrm{Ni}} + k \cdot c \tag{2}$$

where a is the alloy lattice parameter, a_{Ni} is the lattice parameter of pure Ni (0.352 nm), k is a constant equal to 4.5×10^{-2} nm, and c is the atomic fraction of W. As suggested in Ref. [27], Eq. (2) is specifically valid for the interior of grains where diffraction occurs, so c here is interpreted as the grain interior composition (and is not expected to be sensitive to grain boundary composition). Accordingly, by measuring a and using Eq. (2), the grain interior composition can be extracted as shown in Fig. 3, along with literature data for electrodeposited Ni–W [27]. The dotted line represents the trend expected for a homogeneous solid solution; our data fall close to this curve, which suggests that grain boundary segregation in these deposits is subtle at best. The good agreement with results from electrodeposited Ni–W is also encouraging, as grain boundary segregation has been studied in great detail in those alloys [56,57] and indeed found to be very subtle (grain boundary excesses of ~4–8 at.% W). (In contrast, for the strongly segregating Fe–Zr system, a plot such as that of Fig. 3 would reveal the presence of segregation very clearly since the Fe lattice parameter is relatively unchanged as Zr is added [58].)

In summary, Ni–W alloys can be sputter deposited with nanocrystalline, dual-phase nanocrystalline–amorphous, or fully amorphous, microstructures. Of interest here is the range of 0–20 at.% W, where a single-phase solid solution with a constant nanocrystalline grain size is produced. In the subsequent sections, the thick films in this composition range will be used to isolate the effects of solute addition on mechanical properties.

4. Mechanical behavior measurements

The mechanical behavior of the thick Ni–W specimens with 0–20 at.% W was investigated by performing nanoindentation. The reduced modulus, E_R, gives a composite measurement of the elastic properties of the Ni–W films and the diamond indenter tip following [45]:

$$\frac{1}{E_R} = \frac{(1+v_d^2)}{E_d} + \frac{(1+v_f^2)}{E_f} \tag{3}$$

where E is Young's modulus and v is Poisson's ratio, while the subscripts d and f denote properties of the diamond tip and film, respectively. Eq. (3) was used to extract the

Table 2
Microstructure and mechanical properties of sputtered thick Ni–W specimens prepared for nanoindentation (thickness ~1 μm). Note: the change in Burgers vector with composition was accounted for using Eq. (2).

W content (at.%)	Average XRD grain size (nm)	Activation volume (b^3)	Average hardness (GPa)	Average Young's modulus (GPa)
0	20	17	7.2	209
9.1	16	11	8.2	231
13.6	20	17	9.8	242
20	16	14	10.3	253

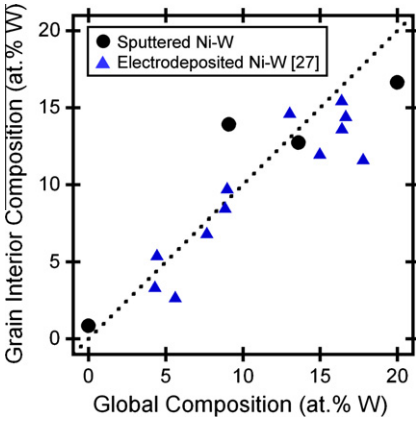

Fig. 3. Grain interior composition determined from X-ray diffraction data using Eq. (2), plotted against global composition. Literature values for electrodeposited Ni–W alloys [27] are included for comparison. The dotted line represents the trend expected for a homogeneous solid solution. Any segregation of W to the grain boundaries in sputtered Ni–W is subtle at best.

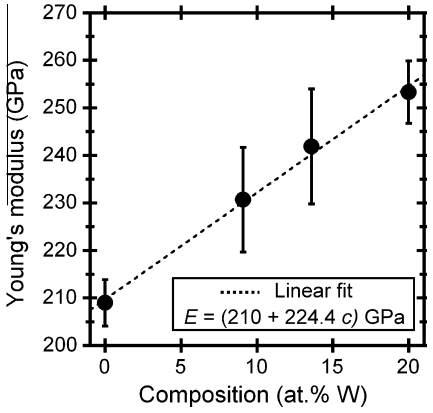

Fig. 4. Young's modulus, measured by nanoindentation, as a function of composition. Modulus increases proportionally to W content.

Young's modulus of the Ni–W films, assuming literature values for the elastic properties of diamond ($E_d = 1140$ GPa; $v_d = 0.07$ [45]) and the Poisson's ratio of Ni ($v_f = 0.31$ [59]). The average Young's modulus for each specimen is presented in Table 2 and plotted against composition in Fig. 4. Inspection of Fig. 4 shows that Young's modulus is 209 GPa for pure Ni, similar to the literature value of 207 GPa [59], and increases proportionally to W content. The increase in Young's modulus with alloying can be traced to the stiff bonds of W, which itself has a Young's modulus of 402 GPa [60] in its bcc phase.

Hardness values were also measured at five indentation strain rates between 0.15 s^{-1} and 15 s^{-1}. The results of these experiments are plotted against strain rate in Fig. 5a, demonstrating that hardness increases with strain rate for all of the compositions. The rate sensitivity of hardness speaks to the dominant physical deformation mechanism, as revealed by calculating the apparent activation volume, V [61,62]:

$$V = \sqrt{3}kT\left(\frac{\partial \ln \dot{\varepsilon}}{\partial \sigma}\right) = 3.8\sqrt{3}\,kT\left(\frac{\partial \ln \dot{\varepsilon}}{\partial H}\right) \quad (4)$$

where k is the Boltzmann constant, T is absolute temperature, $\dot{\varepsilon}$ is strain rate, σ is uniaxial flow stress, and H is hardness (assuming a modified Tabor relation, $H = 3.8\ \sigma$, shown in Ref. [63] for nanocrystalline Ni). Activation volume is the volume over which work is done during a thermally activated event and is a signature of the dominant deformation mechanism. Using Eq. (4), the activation volumes for the Ni–W alloys are calculated, normalized by the cubed Burgers vector (b^3) to facilitate comparison with literature values, and given in Table 2. These values are also plotted in Fig. 5b against literature data for other nanocrystalline metals [18,64–67].

Activation volume decreases from ~1000 b^3 for dislocation forest interactions in microcrystalline metals [68] to much smaller values as intragranular dislocation mechanisms are suppressed through grain refinement. The measured activation volumes for the sputtered alloys lie near the minimum in the activation volume curve observed for grain sizes of ~10–20 nm, and are all between 11 and 17 b^3. These values align well with prior measurements from our group on electrodeposited Ni–W alloys with similar grain sizes [18], and are also consistent with a specific mechanism widely believed to dominate for grains of this size scale: the emission of dislocations from grain boundary sources [66,69,70]. More importantly, the similarity among the activation volumes of our specimens suggests that the same deformation mechanism dominates, regardless of compositional changes.

The fact that the alloys studied here all have the same grain size ($d \sim 18$ nm) and exhibit the same dominant deformation mechanism suggests that any observed trends in mechanical properties with composition can be attributed solely to the effects of solid solution additions; Fig. 5b suggests that the mechanism does not depend on composition, whereas Fig. 5a shows that the hardness strongly does. To better reveal this trend, the hardness measurements in

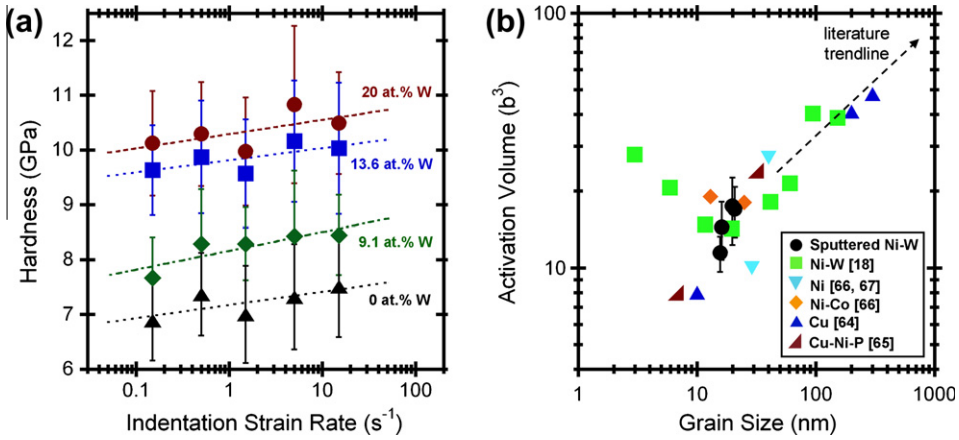

Fig. 5. (a) Hardness as a function of indentation strain rate. For all compositions tested, hardness increases with increasing strain rate. (b) Activation volumes for sputtered Ni–W plotted against grain size, along with literature values for other nanocrystalline metals. The activation volumes are similar for all of the sputtered Ni–W alloys, suggesting that the same physical mechanism dominates deformation regardless of compositional changes. The error bars on activation volume in (b) reflect the standard error of the raw hardness data and the linear regression procedure used to determine $\partial \ln \dot{\varepsilon}/\partial H$.

Fig. 5a were averaged over the five indentation strain rates to facilitate a comparison with respect to alloy composition. These average hardness values are included in Table 2 and plotted against composition in Fig. 6a, where a pronounced strengthening effect is observed as W content increases. The hardness increases from 7.2 GPa for pure Ni to 10.3 GPa for 20 at.% W, an increase of ~43%. To provide a frame of reference, such an improvement is comparable to the increase in strength observed in pure nanocrystalline Ni for grain refinement over almost an order of magnitude, from ~200 to ~40 nm [71]. In addition, this strengthening is much more pronounced than the solid solution strengthening which has been previously reported for coarse-grained Ni–W [72], as shown by the comparison in Fig. 6b (with coarse-grained Ni–W tensile flow stress data from Ref. [72] converted to hardness with a proportionality factor of three). Whereas the literature data for coarse-grained Ni–W reveal sub-GPa levels of strengthening across the accessible solution range, the solution strengthening in the nanocrystalline material is quite substantially larger (up to several GPa).

In the discussion that follows, we will explore the possible origins of this unexpectedly large solid solution strengthening effect in nanocrystalline Ni–W. The insights gained from this dataset are then used to comment more broadly on solid solution effects in nanocrystalline alloys.

5. Discussion

5.1. A new solid solution strengthening mechanism in the nanocrystalline regime

A general scaling law describing the strength of a metal pertains to the spacing and strength of obstacles encountered by dislocations [73,74]:

$$\tau = \frac{F}{bL} \tag{5}$$

where τ is shear strength, F is the restraining force of an obstacle, b is the Burgers vector, and L is the spacing between obstacles. This simple scaling relation can provide key physical insight on the two effects of relevance here: traditional solid solution strengthening and solution strengthening associated with the nanocrystalline grain size.

As a starting point for the discussion, it is useful to revisit the mechanism of traditional solid solution strengthening in coarse-grained alloys, where the relevant obstacles are solute atoms, which influence the elastic energy of a dislocation due to both local size and modulus changes and act as weak obstacles to dislocation motion. There are a number of theories for solid solution strengthening in coarse-grained metals, including the classical Fleischer model [74], which applies mostly for dilute alloys; the Labusch theory [75], which extends the analysis to more concentrated solutions; the Suzuki theory [76], which focuses on chemical effects; as well as other more sophisticated computational models [77,78]. For our purposes, any of these models is sufficient to offer a basic physical view of strengthening, and in fact a simpler model is preferred in order to focus the discussion on the unique effects that emerge in nanostructured alloys. In what follows, we will therefore use the Fleischer model in a schematic sense, and account for coarse-grained solid solution strengthening by directly fitting this model to experimental data.

In the Fleischer formulation for substitutional solutes in cubic metals [74], changes to lattice parameter and shear modulus in the local vicinity of a solute atom are incorporated into an interaction parameter, ε_S, that accounts for the local resistance to dislocation propagation:

$$\varepsilon_S = \left| \frac{\frac{1}{G_{solvent}} \cdot \frac{\partial G}{\partial c}}{1 + \frac{1}{2}\left|\frac{1}{G_{solvent}} \cdot \frac{\partial G}{\partial c}\right|} - 3 \cdot \frac{1}{b_{solvent}} \cdot \frac{\partial b}{\partial c} \right| \tag{6}$$

where G is shear modulus. Based on a combination of empirical observations and mechanistic arguments, Fleischer

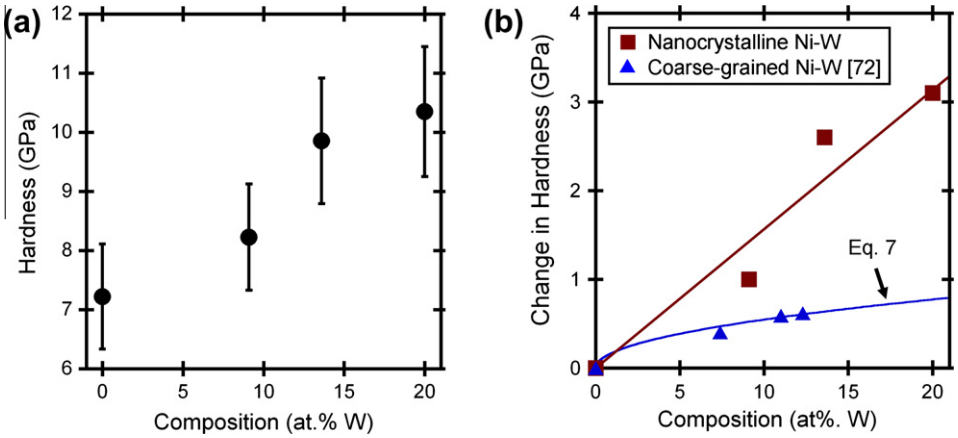

Fig. 6. (a) Hardness, measured by nanoindentation, as a function of composition. Hardness increases significantly with solute addition, increasing by 43% for 20 at.% W. (b) The change in hardness with solute addition, for both coarse-grained [72] and nanocrystalline Ni–W. Nanocrystalline Ni–W demonstrates much more pronounced solid solution strengthening than its coarse-grained counterparts.

found that $F = \alpha G_{solvent} b^2 \varepsilon_S$ (α is a proportionality constant) and $L = b/\sqrt{c\theta}$, where θ is the bending angle of a passing flexible dislocation and is proportional to ε_S [74]. By substituting these terms into Eq. (5), the increase in shear strength due to a solid solution addition in a coarse-grained alloy is predicted by the Fleischer model as:

$$\Delta\tau_{Fleischer} = A \cdot G_{solvent} \cdot \varepsilon_S^{3/2} \cdot c^{1/2} \tag{7}$$

where A is a fitting constant. From literature data for coarse-grained Ni–W solid solutions already shown in Fig. 6b [72], A is empirically fitted as 0.0235. (The interaction parameter is calculated using Eq. (6) with input on the modulus from Fig. 4, lattice parameter from Eq. (2), and using the Poisson's ratio of Ni, $v = 0.31$ [59].) The fit of Eq. (7) to the coarse-grained Ni–W data in Fig. 6b reflects the well-known parabolic dependence upon composition. However, in the case of nanocrystalline Ni–W, solute atoms may no longer be the only relevant obstacles present. Molecular dynamics simulations [79,80], TEM [81], and in situ XRD [1] have suggested that grain boundary dislocation activity dominates deformation in nanocrystalline materials with grain sizes similar to those studied here. A widely accepted strength-limiting mechanism in these materials is a full dislocation (or a complete set of partial dislocations) being emitted from the grain boundary and traversing a grain. For this mechanism the scaling of Eq. (5) still applies, but the dislocations bow between pinning sites within the grain boundaries, such as grain boundary ledges [70]. In this case the dislocation obstacle spacing is essentially the same as the grain size itself, $L = d$, and pinning points at the grain boundary are envisioned to be strong obstacles to dislocation motion, for which $F = Gb^2$. Substituting these terms into Eq. (5), the shear stress, τ_{nc}, required for dislocation motion through nanocrystalline pinning points is given by:

$$\tau_{nc} = \frac{Gb}{d} \tag{8}$$

Asaro et al. [35], as well as others [3,82], have developed expressions along similar lines for nanocrystalline metals. (An alternative but similar mechanism has been proposed, where a leading partial dislocation is emitted from the grain boundary and traverses the entire grain before the trailing partial dislocation is emitted. Such a mechanism was considered but could not explain our observations for the Ni–W system. See Appendix A for a comparison of this partial dislocation model and the nanocrystalline pinning model used here.)

Eq. (8) is a simple scaling relation describing the strength of a nanocrystalline material when the grain size dictates the relevant pinning points for a dislocation process. Accordingly, it is interesting to consider how the simple scaling of Eq. (8) could be affected by the presence of solute. The answer is straightforward: solute additions can affect the strength of a nanocrystalline alloy simply by virtue of their effect on the global properties of the crystal, i.e. by changing the shear modulus, G, and Burgers vector, b, without affecting the controlling deformation mechanism. In other words, nanocrystalline dislocation pinning remains the strength-controlling mechanism, but its potency depends on changes to global shear modulus and Burgers vector, since dislocations are bowing through a medium whose elastic properties have been altered by alloying. In nanocrystalline metals, the inherent strong obstacles to dislocation motion, grain boundaries with nanometer separations, render changes to the global material properties of critical importance, whereas the classical Fleischer model focuses on the local changes of lattice properties around individual solutes.

When applied to a binary alloy, the nanocrystalline pinning model given in Eq. (8) can be decomposed into the contribution of the pure nanocrystalline metal, $\tau_{nc,o}$, and the strengthening increment from solid solution addition, $\Delta\tau_{nc,SS}$:

$$\tau_{nc} = \tau_{nc,o} + \Delta\tau_{nc,SS} \tag{9}$$

where the shear strength due to nanocrystalline pinning in a pure metal is given by:

$$\tau_{nc,o} = \frac{G_{solvent} b_{solvent}}{d} \tag{10}$$

while the strengthening increment from nanocrystalline solution pinning is given by:

$$\Delta\tau_{nc,SS} = \frac{G_{solvent}b_{solvent}}{d}\left[\left(\frac{1}{G_{solvent}}\frac{\partial G}{\partial c}+\frac{1}{b_{solvent}}\frac{\partial b}{\partial c}\right)c + \left(\frac{1}{G_{solvent}}\frac{\partial G}{\partial c}\frac{1}{b_{solvent}}\frac{\partial b}{\partial c}\right)c^2\right] \quad (11)$$

The second term in Eq. (11) is a higher-order combination that is negligible to first order:

$$\Delta\tau_{nc,SS} \approx \frac{G_{solvent}b_{solvent}}{d}\cdot\left(\frac{1}{G_{solvent}}\frac{\partial G}{\partial c}+\frac{1}{b_{solvent}}\frac{\partial b}{\partial c}\right)\cdot c \quad (12)$$

In Eq. (12), the terms in parentheses represent changes to the global lattice properties, and by analogy with Fleischer's construction in Eq. (6), can be termed the interaction parameter for the nanocrystalline solution pinning model:

$$\varepsilon_{nc} = \left(\frac{1}{G_{solvent}}\frac{\partial G}{\partial c}+\frac{1}{b_{solvent}}\frac{\partial b}{\partial c}\right) \quad (13)$$

which permits the nanocrystalline solution pinning effect to be rephrased in terms similar to the Fleischer model, but now with an interaction parameter which encompasses global property changes caused by solutes instead of local dislocation–solute interactions:

$$\Delta\tau_{nc,SS} \approx \frac{G_{solvent}b_{solvent}}{d}\cdot\varepsilon_{nc}\cdot c \quad (14)$$

According to Eq. (14), the composition dependence of nanocrystalline solution pinning is approximately linear in c; note the difference here from the $c^{1/2}$ dependence of the classical Fleischer model. A linear dependence is more in line with our experimental solid solution strengthening data in Fig. 6b. For nanocrystalline Ni–W, we can also note that the change in shear modulus should dominate the strengthening effect, as shear modulus increases by 21% versus only a 2.5% increase of the Burgers vector for the maximum of 20 at.% W.

The total strength of a nanocrystalline alloy should be estimated by combining both of the mechanisms discussed above. Imagining that finely spaced grain boundary pinning points will become more potent due to changes in the global properties of the material, while the Fleischer mechanism will still operate when dislocations encounter individual solutes, we may assume additive contributions from Eqs. (7) and (14) to find the total strengthening from solute addition:

$$\Delta\tau = \Delta\tau_{nc,SS} + \Delta\tau_{Fleischer} \quad (15)$$

which combines with the strength of a pure nanocrystalline metal (Eq. (10)) to give the total shear strength of a nanocrystalline alloy:

$$\tau = \tau_{nc,o} + \Delta\tau_{nc,SS} + \Delta\tau_{Fleischer} \quad (16)$$

The hardness values predicted by Eq. (16) are presented in Fig. 7, along with our experimental measurements of hardness for the sputtered Ni–W system. To calculate the predicted hardness, the average XRD grain size ($d = 18$ nm) and the modified Tabor relation used previously ($H = 3.8\ \sigma$ [63]) are used. Eq. (16) predicts the strength of pure nanocrystalline Ni as well as the observed dependence of strength on W content with surprising accuracy; note that while the Fleischer strengthening contribution (to find the constant A) was calibrated to experimental data from coarse-grained Ni–W in Fig. 6b, the additional contribution for nanocrystalline solution pinning relies on no additional adjustable parameters. These individual contributions are also shown in Fig. 7, demonstrating that neither effect alone is large enough to completely explain the observed strengthening. The grey shaded area in Fig. 7 corresponds to the bounds of the nanocrystalline pinning contribution calculated using values of grain size from 16 to 20 nm, demonstrating that the small uncertainty in our grain sizes does not significantly affect the magnitude of the nanocrystalline pinning contribution or change our conclusions. Both solid solution strengthening mechanisms must be accounted for in these alloys.

5.2. Consequences of the new solid solution effect

The above section showed that in nanocrystalline alloys, traditional Fleischer strengthening is augmented by a new solid solution mechanism where the alloying affects the global properties of the lattice, which in turn affects the yield strength. In the simplest terms, Eq. (14) can be interpreted in the following way: in nanocrystalline alloys, elements which stiffen the lattice (i.e. have a positive value of $\partial G/\partial c$) or expand it (i.e. have a positive value of $\partial b/\partial c$) increase the stress needed to reach the yield strain. In cases where the alloying element is significantly stiffer, as for W in Ni, the strengthening effect can be very large, as seen in our

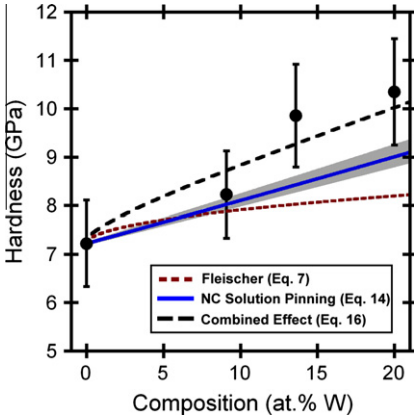

Fig. 7. Hardness for nanocrystalline Ni–W as a function of W content, along with predictions based on Fleischer strengthening, nanocrystalline solution pinning strengthening, and a combination of the two effects. Neither model can explain the observed strengthening by itself, but the combination of the two effects provides a good match to the experimental results. The grey shaded area corresponds to the bounds of the nanocrystalline pinning contribution calculated using values of grain size from 16 to 20 nm, demonstrating that the small uncertainty in our grain sizes does not significantly affect the magnitude of the nanocrystalline pinning contribution.

data in Fig. 7. However, an interesting implicit prediction not immediately apparent from our discussion of Ni–W is that alloying can lead to negligible strengthening if $\partial G/\partial c$ is small, and, in fact, can lead to solid solution softening when $\partial G/\partial c$ is negative. This stands in contrast to traditional solid solution strengthening models, which exhibit the well-known characteristic that they often expect hardening regardless of whether the solute element is stiffer or more compliant than the solvent.

An example of such behavior is shown in Fig. 8a, where the shear strength of single crystalline Ni–Cu increases with Cu content [83] in a manner that can be accurately described by the Fleischer strengthening model (Eq. (7)). Even though Cu has a significantly lower shear modulus than Ni, strengthening is observed. Alternatively, the nanocrystalline solution pinning mechanism (Eq. (14)) predicts solid solution softening for nanocrystalline Ni–Cu alloys, due to the decreasing global shear modulus. Microhardness data from Ref. [84] for Ni–Cu alloys with grain sizes of ~20 nm is shown in Fig. 8b, and indeed does show softening with Cu addition. This trend can be well-described by Eq. (15), with the softening predicted by the nanocrystalline solution pinning term dominating the overall solid solution effect in this case. The predictions shown in Fig. 8b, based on Eq. (15), take their input from Refs. [59,83], and again involve no adjustable parameters.

To show that the solid solution effects captured in Eq. (15) apply broadly to many nanocrystalline alloys, data from the Pt–Ru [85], Ni–Co [86], and Fe–Cu [84] systems are added to those discussed above in Fig. 9. These systems were chosen from the relatively large number of experimental works on nanocrystalline alloy systems, because these studies exhibit the unique property of collecting systematic data at several solid solution compositions at a roughly constant grain size. Details about the structure and production of the chosen alloys are presented in Table 3. Fig. 9 shows the measured change in hardness with solute addition for these alloys, along with the predicted trends from Eq. (15). (Reliable data for the solution hardening of coarse-grained Fe–Cu alloys could not be found due to the extremely limited solubility of Cu in Fe [87]. Therefore, for the Fe–Cu system, only the effect of the nanocrystalline solution pinning model is accounted for here.) From the close agreement between Eq. (15) and the experimental data, we believe that our discussion has identified the controlling physical solute effects for a wide range of nanocrystalline alloys, capturing everything from strong strengthening for Pt–Ru to softening for Ni–Cu and Fe–Cu.

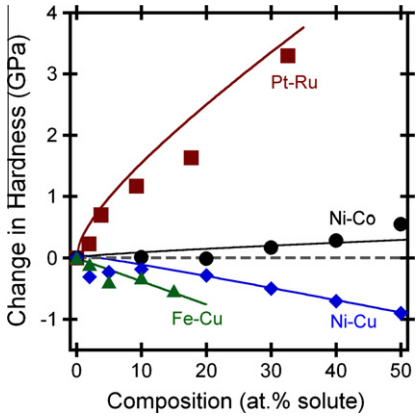

Fig. 9. The change in hardness with solute addition for nanocrystalline Pt–Ru [85], Ni–Co [86], Ni–Cu [84], and Fe–Cu [84] alloys. In all four cases, the observed solution effects can be predicted by the combined solid solution model presented in Eq. (15). Predictions from Eq. (15) are shown as solid lines.

5.3. Critical grain sizes for solid solution effects

Comparison of the two models for solid solution strengthening (Eqs. (7) and (14)) also shows that nanocrystalline solution strengthening has a dependence on grain size while classical Fleischer strengthening does not. Therefore, a critical grain size exists where the solid solution effect predicted by both models is of equal magnitude, separating regimes of dominance for the two effects. This is shown in Fig. 10a, where the results of both models are

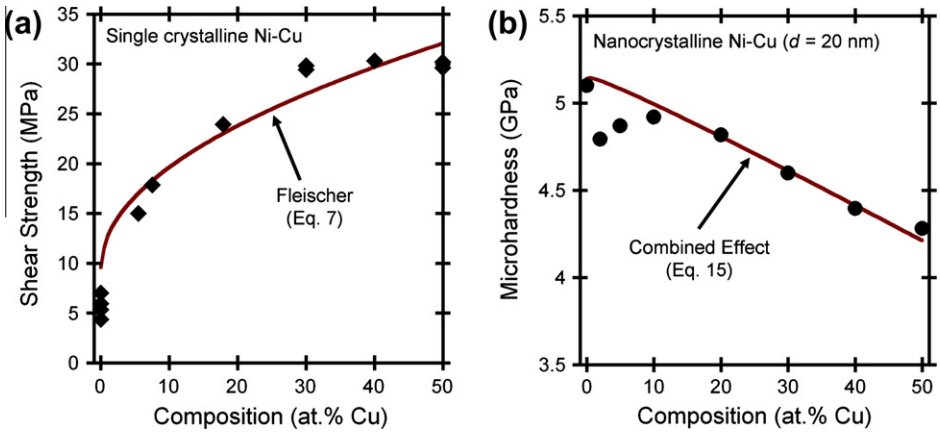

Fig. 8. (a) Shear strength of single crystalline Ni–Cu [83], showing solid solution hardening even for a more compliant solute addition. Such behavior is predicted by traditional models, such as the Fleischer model (Eq. (7)). (b) Nanocrystalline Ni–Cu alloys [84], however, show solid solution softening in line with predictions based on a combination of the nanocrystalline solution pinning model and the Fleischer model (Eq. (15)).

Table 3
Microstructure and processing history of nanocrystalline alloys included in Fig. 9.

Elemental system	Reference	Grain size (nm)	Crystal structure	Production method	Reference for coarse-grained solution strengthening
Pt–Ru	[85]	33	fcc	Sputtering	[59]
Ni–Co	[86]	16	fcc	Ball milling	[90]
Ni–Cu	[84]	20	fcc	Ball milling	[83]
Fe–Cu	[84]	16	bcc	Ball milling	

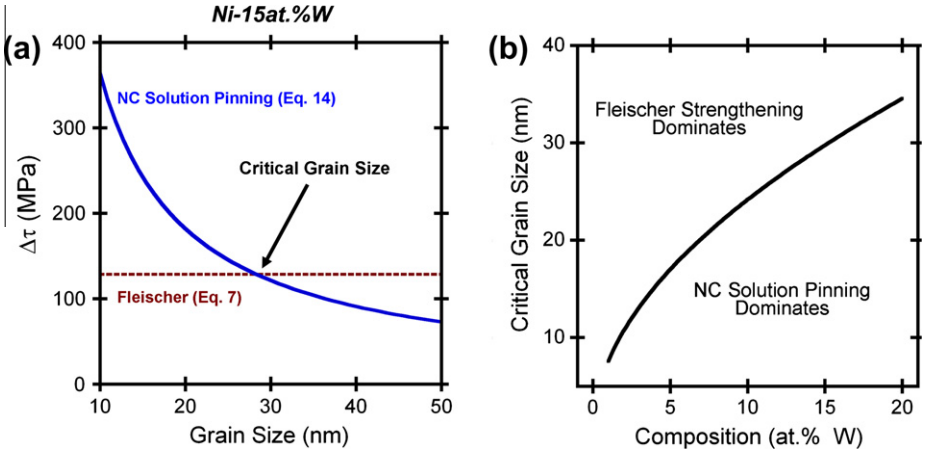

Fig. 10. (a) Strength increase for Ni–15 at.% W from the nanocrystalline solution pinning and Fleischer models, showing that a critical grain size exists where the strengthening predicted by the models is equal. For grain sizes below this critical value, the nanocrystalline solution pinning term dominates the strengthening effect. (b) The critical grain size is plotted against composition, showing that nanocrystalline solution pinning strengthening dominates for smaller grain sizes and larger amounts of W addition.

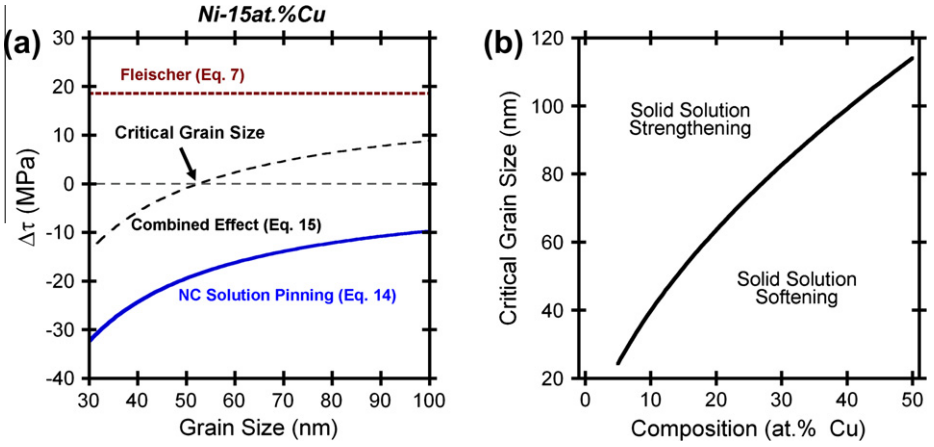

Fig. 11. (a) Solution effects for Ni–15 at.% Cu from the nanocrystalline solution pinning and Fleischer models, showing that a critical grain size exists where the two contributions cancel out, resulting in zero net effect. For grain sizes below this critical value, a softening effect occurs. (b) The critical grain size is plotted against composition, showing that solid solution softening occurs for smaller grain sizes and larger amounts of Cu addition.

plotted as a function of grain size for Ni containing 15 at.% W. It is only at grain sizes below the cross-over ($d_c = 29$ nm here) that the new contribution from nanocrystalline solution pinning becomes dominant, whereas the classical Fleischer effect dominates at larger grain sizes. The critical grain size can be calculated from Eqs. (7) and (14) as:

$$d_c = \left(\frac{b_{solvent}}{A} \cdot \frac{|\varepsilon_{nc}|}{\varepsilon_S^{3/2}} \right) \cdot c^{1/2} \tag{17}$$

The critical grain size for Ni–W is plotted against composition in Fig. 10b, showing that the nanocrystalline solution pinning mechanism dominates strengthening for smaller grain sizes and larger amounts of solute addition.

In cases where the nanocrystalline solution pinning term predicts softening (e.g. for Ni–Cu), the critical grain size represents the point at which the softening from the nanocrystalline solution pinning model equals the strengthening from the Fleischer model, resulting in no net effect of alloy-

ing upon strength. This is shown in Fig. 11a, where the two strengthening terms and the total combined effect are plotted as a function of grain size for Ni–15Cu (at.%). For grain sizes below this critical value, an overall softening is predicted. The critical grain size for Ni–Cu is plotted against composition in Fig. 11b, demonstrating that solute softening should occur for smaller grain sizes and larger amounts of solute addition. For the case where nanocrystalline solution pinning causes a softening effect which competes with Fleischer strengthening, the sign of the net solid solution effect can be predicted using Eq. (17).

6. Conclusions

Sputtered Ni–W has been used as a model system to study solid solution strengthening in nanocrystalline alloys. The results presented here allow the following conclusions to be made:

- The microstructure of sputtered Ni–W alloys transitions from nanocrystalline to amorphous–nanocrystalline composite to fully amorphous as W content is increased. Since a constant nanocrystalline grain size is found over a broad range of compositions from 0 to 20 at.% W, these alloys can be used to decouple solid solution strengthening from grain size effects.
- Substitutional solute addition alone can significantly increase the strength of nanocrystalline alloys; in the case of Ni–W, we observe an increase in hardness of ~43%, amounting to 3.1 GPa, as W content increases to ~20 at.%. The increase appears roughly linear in composition, and is much larger than expected for traditional dislocation–solute interaction models.
- A model based on dislocation pinning at nanocrystalline grain boundaries can provide the missing link for predicting solid solution strengthening in nanocrystalline alloys. For such a mechanism, the effect of solute addition on the global average elastic modulus is of primary importance. When this nanocrystalline solution pinning model is combined with the traditional Fleischer model, the strengths of Ni and Ni–W alloys with grain sizes of ~20 nm can be accurately described.
- The combined solid solution model presented here can predict the solid solution strengthening or softening behavior of a number of nanocrystalline alloys. The ability to predict the softening which has been observed for some nanocrystalline systems, namely those where the solutes are more compliant than the matrix, is particularly interesting, as traditional models predict strengthening with solute addition for these systems.
- Due to the grain size dependence of the nanocrystalline solution pinning term, a critical grain size can be found where the contribution of this unique nanocrystalline deformation mechanism is equal to that of the traditional Fleischer mechanism. Depending on whether the two mechanisms work together or compete, this critical value allows the dominant contribution to strengthening or the net solid solution effect (strengthening versus softening) to be found.

Taken as a whole, our work shows that alloying additions significantly influence the mechanical response of nanocrystalline metals. The experimental results presented here isolate the effects of solute addition on mechanical behavior, showing that solid solution strengthening in nanocrystalline metals can be significantly different from expectations based on traditional solid solution strengthening models.

Acknowledgements

This work was supported by the US Army Research Office, through Grant W911NF-09-1-0422 and through the Institute for Soldier Nanotechnologies at MIT.

Appendix A

A.1. Effect of alloying on stacking fault energy

A secondary effect of alloying not discussed in the main body of the paper is upon the stacking fault energies, which can affect the strength of nanocrystalline metals. Consider, for example, an adaptation of the strength-limiting mechanism described in the paper (in which a full dislocation or complete set of partial dislocations is emitted from the grain boundary and traverses the grain). Asaro et al. [35] proposed that in some cases a leading partial dislocation will be emitted from the grain boundary and traverse the entire grain before the trailing partial dislocation is emitted, as observed in molecular dynamics simulations [88] and thought to be responsible for deformation twinning in nanocrystalline Al [2]. The required shear stress, $\tau_{Partial}$, for deformation dominated by partial dislocation emission is given by Asaro et al. as [35]:

$$\frac{\tau_{Partial}}{G} = \left(\frac{1}{3} - \frac{1}{12\pi}\right)\frac{b}{d} + \frac{\gamma_{SF}}{Gb} \tag{A1}$$

where γ_{SF} is the stacking fault energy.

For our sputtered Ni–W alloys, d is constant while b increases only slightly with W addition, with Eq. (2) predicting an increase in b of ~2.5% for 20 at.% W. As such, τ/G should be relatively constant for our alloys if deformation can be described by the simple nanocrystalline solution pinning model (Eq. (8)). The relationship between γ_{SF} and composition for Ni–W alloys is presented in Fig. A1a, with data taken from Ref. [89]. As W is added in solid solution to fcc Ni, the stacking fault energy drops rapidly from an initial value 235 mJ m^{-2} and approaches a plateau of ~50 mJ m^{-2}. While the first term in Eq. (A1) will be relatively constant, similar to Eq. (8), the second term is a strong negative function of composition since γ_{SF} decreases and G increases with W content. Accordingly, τ/G should quickly fall with W addition for our alloys if partial dislocation emission dominates plasticity.

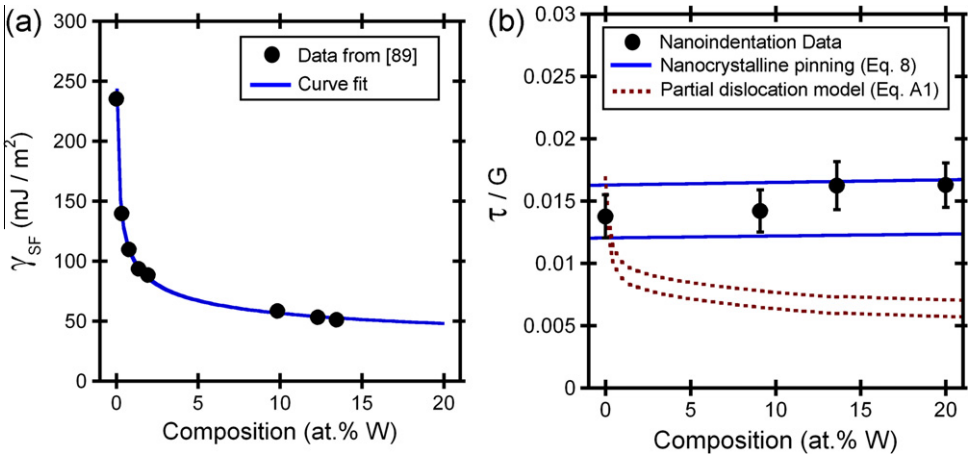

Fig. A1. (a) Stacking fault energy of Ni–W alloys as a function of composition [89]. (b) τ/G calculated from nanoindentation experiments, compared with predictions based on grain boundary emission of full dislocations (Eq. (8)) or lead partial dislocations and stacking faults only (Eq. (A1)). Based on the agreement between the nanoindentation data and Eq. (8), it is concluded that plastic deformation in these alloys is best described by the nanocrystalline solution pinning model.

The values of τ/G calculated from our indentation experiments are presented in Fig. A1b, along with predictions based on Eqs. (8) and (A1). For the predicted curves, we use the average measured XRD grain size of $18\text{ nm} \pm 15\%$ (to account for XRD error) to calculate upper and lower bounds for each model. Our experimental results for τ/G are relatively constant with respect to W content (although a subtle increase can be observed due to the small increase in b and the Fleischer model's contribution to strengthening), results which are in line with the predictions based on a mechanism of full dislocations or pairs of partial dislocations interacting with grain boundary ledges. On the other hand, the predictions based on partial dislocations fully traversing the grain quickly fall off as W is added and significantly underestimate the experimental τ/G values.

References

[1] Budrovic Z, Van Swygenhoven H, Derlet PM, Van Petegem S, Schmitt B. Science 2004;304:273.
[2] Chen MW, Ma E, Hemker KJ, Sheng HW, Wang YM, Cheng XM. Science 2003;300:1275.
[3] Cheng S, Spencer JA, Milligan WW. Acta Mater 2003;51:4505.
[4] Schiotz J, Di Tolla FD, Jacobsen KW. Nature 1998;391:561.
[5] Van Swygenhoven H, Derlet PA. Phys Rev B 2001;64:9.
[6] Cahn JW, Mishin Y, Suzuki A. Acta Mater 2006;54:4953.
[7] Cahn JW, Taylor JE. Acta Mater 2004;52:4887.
[8] Legros M, Gianola DS, Hemker KJ. Acta Mater 2008;56:3380.
[9] Dao M, Lu L, Asaro RJ, De Hosson JTM, Ma E. Acta Mater 2007;55:4041.
[10] Weertman JR, Farkas D, Hemker K, Kung H, Mayo M, Mitra R, et al. MRS Bull 1999;24:44.
[11] Padilla HA, Boyce BL. Exp Mech 2010;50:5.
[12] Farhat ZN, Ding Y, Northwood DO, Alpas AT. Mater Sci Eng A 1996;206:302.
[13] Jeong DH, Gonzalez F, Palumbo G, Aust KT, Erb U. Scr Mater 2001;44:493.
[14] Rupert TJ, Schuh CA. Acta Mater 2010;58:4137.
[15] Gianola DS, Warner DH, Molinari JF, Hemker KJ. Scr Mater 2006;55:649.
[16] Schwaiger R, Moser B, Dao M, Chollacoop N, Suresh S. Acta Mater 2003;51:5159.
[17] Lund AC, Schuh CA. Acta Mater 2005;53:3193.
[18] Trelewicz JR, Schuh CA. Acta Mater 2007;55:5948.
[19] Ames M, Markmann J, Karos R, Michels A, Tschope A, Birringer R. Acta Mater 2008;56:4255.
[20] Gertsman VY, Birringer R. Scr Metall Mater 1994;30:577.
[21] Jin M, Minor AM, Stach EA, Morris JW. Acta Mater 2004;52:5381.
[22] Zhang K, Weertman JR, Eastman JA. Appl Phys Lett 2004;85:5197.
[23] Koch CC, Scattergood RO, Darling KA, Semones JE. J Mater Sci 2008;43:7264.
[24] Weissmuller J. Nanostruct Mater 1993;3:261.
[25] Detor AJ, Schuh CA. J Mater Res 2007;22:3233.
[26] Detor AJ, Schuh CA. Acta Mater 2007;55:4221.
[27] Detor AJ, Schuh CA. Acta Mater 2007;55:371.
[28] Liu F, Kirchheim R. J Cryst Growth 2004;264:385.
[29] Krill CE, Klein R, Janes S, Birringer R. Mater Sci Forum 1995;179:443.
[30] Li HQ, Ebrahimi F. Mater Sci Eng A-Struct Mater Prop Microstruct Process 2003;347:93.
[31] Han BQ, Lavernia EJ. Adv Eng Mater 2005;7:457.
[32] Scattergood RO, Koch CC, Murty KL, Brenner D. Mater Sci Eng A 2008;493:3.
[33] Schuh CA, Nieh TG, Iwasaki H. Acta Mater 2003;51:431.
[34] Argon AS, Yip S. Philos Mag Lett 2006;86:713.
[35] Asaro RJ, Krysl P, Kad B. Philos Mag Lett 2003;83:733.
[36] Van Swygenhoven H, Derlet PM, Froseth AG. Nat Mater 2004;3:399.
[37] Yamakov V, Wolf D, Phillpot SR, Mukherjee AK, Gleiter H. Nat Mater 2004;3:43.
[38] Brett CMA, Cavaleiro A. Thin Solid Films 1998;322:263.
[39] Kawashima A, Akiyama E, Habazaki H, Hashimoto K. Mater Sci Eng A 1997;226:905.
[40] Metikos-Hukovic A, Grubac Z, Radic N, Tonejc A. J Mol Catal A 2006;249:172.
[41] Pai CS, Lau SS, Poker DB, Hung LS. J Appl Phys 1985;58:4172.
[42] Szklarska-Smialowska Z, Shademan S, Inturi R. Effect of Cr, W and Ta on the pitting potential of sputtered Ni-alloys. In: Heusler KE, editor. Passivation of metals and semiconductors, vol. 185–188; 1995. p. 1011.
[43] Zhu MF, Suni I, Nicolet MA, Sands T. J Appl Phys 1984;56:2740.
[44] Cullity BD. Elements of X-ray diffraction. Reading (MA): Addison-Wesley; 1959. p. 262.
[45] Oliver WC, Pharr GM. J Mater Res 2004;19:3.
[46] Lucas BN, Oliver WC. Metall Mater Trans A 1999;30:601.

[47] Gianola DS, Van Petegem S, Legros M, Brandstetter S, Van Swygenhoven H, Hemker KJ. Acta Mater 2006;54:2253.
[48] Gabriel A, Lukas HL, Allibert CH, Ansara I. Z Metallkd 1985;76:589.
[49] Eastman JA, Thompson LJ, Kestel BJ. Phys Rev B 1993;48:84.
[50] Meng QP, Rong YH, Hsu TY. Mater Sci Eng A 2007;471:22.
[51] da Silva M, Wille C, Klement U, Choi P, Al-Kassab T. Mater Sci Eng A 2007;445:31.
[52] Liu F. Appl Phys A 2005;81:1095.
[53] Hirotsu Y, Ohkubo T, Matsushita M. Microsc Res Tech 1998;40:284.
[54] Chan KY, Tou TY, Teo BS. Microelectron J 2006;37:608.
[55] Nagender Naidu SV, Rama Rao P. Phase diagrams of binary tungsten alloys. Calcutta, India: Indian Institute of Metals; 1991.
[56] Detor AJ, Miller MK, Schuh CA. Philos Mag 2006;86:4459.
[57] Detor AJ, Miller MK, Schuh CA. Philos Mag Lett 2007;87:581.
[58] Darling KA, Chan RN, Wong PZ, Semones JE, Scattergood RO, Koch CC. Scr Mater 2008;59:530.
[59] Metals handbook, vol. 2 – properties and selection: nonferrous alloys and pure metals. Metals Park (OH): American Society for Metals; 1989.
[60] Lowrie R, Gonas AM. J Appl Phys 1965;36:2189.
[61] Kocks UF, Argon AS, Ashby MF. Prog Mater Sci 1975;19:1.
[62] Taylor G. Prog Mater Sci 1992;36:29.
[63] Dalla Torre F, Van Swygenhoven H, Victoria M. Acta Mater 2002;50:3957.
[64] Chen J, Lu L, Lu K. Scr Mater 2006;54:1913.
[65] Chen J, Shi YN, Lu K. J Mater Res 2005;20:2955.
[66] Lian JS, Gu CD, Jiang Q, Jiang ZH. J Appl Phys 2006;99:3.
[67] Wang YM, Hamza AV, Ma E. Acta Mater 2006;54:2715.
[68] Conrad H. Mater Sci Eng A 2003;341:216.
[69] Asaro RJ, Suresh S. Acta Mater 2005;53:3369.
[70] Van Swygenhoven H, Derlet PM, Froseth AG. Acta Mater 2006;54:1975.
[71] Ebrahimi F, Bourne GR, Kelly MS, Matthews TE. Nanostruct Mater 1999;11:343.
[72] Pelloux RMN, Grant NJ. Trans Am Inst Min Metall Eng 1960;218:232.
[73] Courtney TH. Mechanical behavior of materials. New York, NY: McGraw-Hill; 2000.
[74] Fleischer RL. Solid-solution hardening. In: Peckner D, editor. The strengthening of metals. New York, NY: Reinhold Publishing Corp.; 1964. p. 93.
[75] Labusch R. Phys Status Solidi 1970;41:659.
[76] Suzuki H. The yield strength of binary alloys. In: Fisher JC, editor. Dislocations and mechanical properties of crystals. New York: J. Wiley; 1957. p. 361.
[77] Leyson GPM, Curtin WA, Hector LG, Woodward CF. Nat Mater 2010;9:750.
[78] Proville L, Patinet S. Phys Rev B 2010:82.
[79] Derlet PM, Van Swygenhoven H, Hasnaoui A. Philos Mag 2003;83:3569.
[80] Yamakov V, Wolf D, Phillpot SR, Mukherjee AK, Gleiter H. Nat Mater 2002;1:45.
[81] Kumar KS, Suresh S, Chisholm MF, Horton JA, Wang P. Acta Mater 2003;51:387.
[82] Arzt E. Acta Mater 1998;46:5611.
[83] Osswald E. Z Phys 1933;83:55.
[84] Shen TD, Koch CC. Acta Mater 1996;44:753.
[85] Hyun S, Kraft O, Vinci RP. Acta Mater 2004;52:4199.
[86] Shen TD, Koch CC. Mater Sci Forum 1995;179–181:17.
[87] Metals Handbook, vol. 3 – alloy phase diagrams. Metals Park, OH: American Society for Metals; 1992.
[88] Van Swygenhoven H, Spaczer M, Caro A. Acta Mater 1999;47:3117.
[89] Tiearney TC, Grant NJ. Metall Trans A 1982;13:1827.
[90] Davies CKL, Sagar V, Stevens RN. Acta Metall 1973;21:1343.